Nanoscale Horizons

Check for updates

A conductive framework embedded with cobalt-doped vanadium nitride as an efficient polysulfide adsorber and convertor for advanced lithium–sulfur batteries†

Yang Lu, [ID] ‡*[a] Menglong Zhao,‡[a] Ya Yang, [ID][a] Mengjie Zhang,[a] Ning Zhang,[a] Hailong Yan,[a] Tao Peng,[a] Xianming Liu [ID][b] and Yongsong Luo [ID] *[ac]

The industrialization and commercialization of Li–S batteries are greatly hindered by several defects such as the sluggish reaction kinetics, polysulfide shuttling and large volume expansion. Herein, we propose a heteroatom doping method to optimize the electronic structure for enhancing the adsorption and catalytic activity of VN that is *in situ* embedded into a spongy N-doped conductive framework, thus obtaining a Co-VN/NC multifunctional catalyst as an ideal sulfur host. The synthesized composite has both the unique structural advantages and the synergistic effect of cobalt, VN, and nitrogen-doped carbon (NC), which not only improve the polysulfide anchoring of the sulfur cathode but also boost the kinetics of polysulfide conversion. The density functional theory (DFT) calculations revealed that Co doping could enrich the d orbit electrons of VN for elevating the d band center, which improves its interaction with lithium polysulfides (LiPSs) and accelerates the interfacial electron transfer, simultaneously. As a result, the batteries present a high initial discharge capacity of 1521 mA h g^{-1} at 0.1 C, good rate performance, and excellent cycling performances ($\sim$876 mA h g^{-1} at 0.5 C after 300 cycles and $\sim$490 mA h g^{-1} at 2 C after 1000 cycles, respectively), even with a high areal sulfur loading of 4.83 mg cm^{-2} ($\sim$4.70 mA h cm^{-2} at 0.2 C after 100 cycles). This well-designed work provides a good strategy to develop effective polysulfide catalysis and further obtain high-performance host materials for Li–S batteries.

New concepts

Smooth trapping, diffusion and conversion of lithium polysulfides by various catalysts is a promising strategy for restraining the shuttle effect in Li–S batteries. However, most conventional catalysts have their own inevitable drawbacks that reduce the capture or conversion efficiency of LiPSs. Heteroatom doping is an effective modification method to complement the shortcomings of catalysts. In this work, we design a cobalt-doped vanadium nitride nanocrystal embedded in a conductive carbon framework, aiming to simultaneously enhance the adsorption and catalytic performance of VN catalysts for polysulfides. Density functional theory calculations and experimental results jointly demonstrated the enriched d orbit electrons and embellished bandgap of VN by cobalt doping, further improving the reaction kinetic behaviors of LiPSs. This heteroatom doping strategy provides a unique insight for constructing catalysts with optimized adsorption and interfacial charge transfer capability in Li–S batteries.

Introduction

To create a sustainable, resource efficient and carbon-neutral society, more economical and higher energy density battery technologies are needed urgently.[1,2] Lithium–sulfur (Li–S) batteries have been regarded as one of the key next-generation energy storage systems in the past few decades, due to their high theoretical specific capacity (1675 mA h g^{-1}), remarkable energy density (2600 W h kg^{-1}) and abundant resources of sulfur.[3] Although there are many advantages, the shuttle effect of soluble lithium polysulfides (LiPSs) and sluggish reaction kinetics have greatly hindered the commercialization of Li–S batteries, which are caused by the intrinsic liquid–solid phase reaction of LiPSs to Li$_2$S$_2$/Li$_2$S and multistep electron conversion processes.[4,5] These obstacles lead to the irreversible loss of sulfur and serious anode corrosion, which exacerbate the poor rate performance and rapid capacity decay during long-term cycling conditions.[6,7] Therefore, various catalysts, including sulfides, oxides, nitrides and phosphides, have been widely investigated to enhance the reaction kinetics in Li–S batteries.[8–11]

[a] Henan Joint International Research Laboratory of New Energy Storage Technology, Key Laboratory of Microelectronics and Energy of Henan Province, School of Physics and Electronic Engineering, Xinyang Normal University, Xinyang 464000, P. R. China. E-mail: luyang.181@163.com, ysluo@xynu.edu.cn; Fax: +86 376 6390801; Tel: +86 376 6390801

[b] College of Chemistry and Chemical Engineering, Luoyang Normal University, Luoyang 471934, P. R. China

[c] College of Physics and Electronic Engineering, Nanyang Normal University, Nanyang 473061, P. R. China

† Electronic supplementary information (ESI) available. See DOI: 10.1039/d1nh00512j

‡ Yang Lu and Menglong Zhao contributed equally to this work.

Among these candidates, vanadium nitride (VN) stands out as one of the most promising sulfur host materials because of its robust electrochemical corrosion resistance and remarkable electronic conductivity (1.17×10^6 S m^{-1} at room temperature)[12] More significantly, VN possesses similar catalytic properties to noble metals that may facilitate the conversion from long-chain polysulfides (Li$_2$S$_n$, $n \geq 4$) to short-chain Li$_2$S$_2$/Li$_2$S and further improve the reaction kinetics.[12] Nevertheless, owing to the anion species occupying the interstitial sites of lattices, the trapping ability toward LiPSs of metal nitrides is much weaker than that of metal oxides, leading to a compromise of trapping and conversion efficiency.[13,14] To enhance the adsorption ability of VN with LiPSs, Co atom doping is a promising material modification strategy, which could engineer the electronic structure by increasing d electrons.[15–17] However, Co-doped VN has a strong tendency of aggregation through hydrothermal reaction, and this large-size electrocatalyst with a limited area of the reactive interface leads to the partial loss of sulfur active material.[18,19] In consequence, the synthesis of ideal catalysts with smaller particle sizes, richer reaction interfaces, appropriate adsorption ability and ultra-high catalytic activity remains a critical challenge.

With careful consideration of the metal heteroatom doping effect and catalyst interface design, a N-doped graphitic carbon framework embedded with Co-VN nanocrystals (Co-VN/NC) is synthesized as an efficient polysulfide adsorber and convertor through a facile template-assisted strategy. Here, the NaCl crystal as a template can be removed by deionized water, the glucose acted as a C source to structure the 3D porous carbon framework, and the NH$_4$VO$_3$, urea and Co(NO$_3$)$_2$·6H$_2$O were the V, N and Co source, respectively. Notably, the introduction of Co element could enrich the d orbit electrons of VN, and further redistribute the d-band center and embellish the bandgap, which can improve the affinity toward LiPSs. Moreover, the widespread ultrasmall Co-VN particles offer abundant triple-phase interfaces (between catalyst, conductive substrate and electrolyte) for rapid surface reactions of LiPSs and accelerating Li$_2$S uniform nucleation and growth. Furthermore, the N doping of the graphitic carbon conductive network provides more electric contact sites for rapid surface electronic exchange, and improves the surface wettability for reducing the polarization resistance of the sulfur cathode. As a result, the 3D Co-VN/NC cathodes yield a remarkable cycling performance with a decay rate of 0.043% per cycle over 1000 cycles at 2.0 C, and delivered a high areal capacity of 4.98 mA h cm^{-2} even with a sulfur loading of 4.83 mg cm^{-2}.

Experimental section

Template-assisted fabrication of the 3D Co-VN/NC framework

In a typical synthesis process, NaCl (10 g), glucose (2 g), urea (1 g), NH$_4$VO$_3$ (0.6 g) and Co(NO$_3$)$_2$·6H$_2$O (0.05 g) were dissolved into 100 ml of deionized (DI) water, respectively. After vigorous ultrasonic stirring for 2 h, the transparent solution was frozen in a refrigerator and the water was removed via freeze-drying at −50 °C. And then, the obtained precursor was mixed with melamine in a mass ratio of 1 : 1 for subsequent nitriding. Afterwards, the mixture was put into a porcelain boat with a cover and calcined at 700 °C for 4 h under an Ar atmosphere with a heating rate of 5 °C min^{-1}. Finally, the resultant black product was filtrated with DI water to dissolve the NaCl crystals, and subsequently dried in a vacuum oven at 60 °C. Meanwhile, the 3D VN/NC was synthesized under a similar procedure without Co(NO$_3$)$_2$·6H$_2$O, and the 3D NC was obtained by normal annealing under Ar atmosphere, without the addition of Co(NO$_3$)$_2$·6H$_2$O, NH$_4$VO$_3$ or melamine for comparison.

Synthesis of Co-VN/NC/S, VN/NC/S and NC/S cathodes

Sulfur was infiltrated into the porous carbon networks through the conventional melt-diffusion method. Each of the carbon materials was ground with sublimed sulfur in a weight ratio of 2 : 8, sealed into a glass tube under an Ar atmosphere, and heated to 155 °C for 12 h.

Visualized adsorption test

5 mmol L^{-1} Li$_2$S$_6$ solution was prepared by dissolving sulfur and Li$_2$S at a molar ratio of 5 : 1 in 1,2-dimethoxyethane (DME) and 1,3-dioxolane (DOL) (1 : 1, ratio by volume). Then, 5 mg Co-VN/NC, VN/NC and NC were added into 3 mL Li$_2$S$_6$ solution, separately. The mixture adsorption tests were executed in an argon-filled glove box.

Assembly of symmetric cells

Sulfur and Li$_2$S with a molar ratio of 5 : 1 were dissolved in a DOL/DME solution (1 : 1, ratio by volume) containing 1 M Lithium bis-trifluoromethanesulfonylimide (LiTFSI) and 0.1M LiNO$_3$ to prepare 0.2 mol L^{-1} Li$_2$S$_6$ solution. The Co-VN/NC, VN/NC and NC powder was dispersed in ethanol under ultrasonication and the dispersion was added dropwise onto carbon paper (the mass loading is 0.5 mg cm^{-2}). Two identical electrodes were assembled into a coin-type cell with a Celgard 2500 membrane and 20 µL Li$_2$S$_6$-based electrolyte.

Tests for the Li$_2$S nucleation

0.2 mol L^{-1} Li$_2$S$_8$ solution was prepared by dissolving Li$_2$S and S powder (molar ratio of 1 : 7) into Li–S electrolyte under vigorous stirring at 60 °C for 24 h. The Co-VN/NC, VN/NC or NC powder (1 mg cm^{-2}) was loaded onto carbon paper as the cathode and lithium foil was used as the anode. 25 µL Li$_2$S$_8$ electrolyte was dropped onto the cathode and then 20 µL blank Li–S electrolyte was dropped on the lithium anode side. The assembled batteries were discharged to 2.12 V under a constant current of 112 µA, and then discharged potentiostatically at 2.10 V until the current dropped below 10 µA for Li$_2$S deposition. According to Faraday's law, the whole charge was collected to estimate the capacity of Li$_2$S precipitation.

Material characterization

SEM was executed by a Hitachi S-4800 instrument. TEM measurement was performed on a transmission electron microscope (FEI Tecnai G2 F20) coupled with an energy dispersive

spectrometer (EDS). XRD patterns were identified on a Bruker D-8 diffractometer with Cu Kα ($\lambda = 0.154$ nm) radiation at room temperature. XPS spectra were recorded through a K-Alpha 0.5 eV (Thermo Scientific) XPS system. Raman spectroscopy was conducted on a Renishaw Instruments INVIA Raman microprobe with a 532 nm laser source. The surface area measurement was conducted by Brunauer–Emmett–Teller analysis on a Physical & Chemical Adsorption system (ASAP 2460). The sulfur and Co-VN content of the composites was analyzed by TGA (Netzsch STA499f5) at a heating rate of 10 °C min^{-1} in an Ar or Air atmosphere. Ultraviolet-visible (UV-Vis) tests were executed on a UV/Vis spectrophotometer (Hitachi U-3900H).

Electrochemical measurements

The cathodes were prepared by mixing Co-VN/NC/S powder (80 wt%), acetylene black (10 wt%) and poly(vinylidene fluoride) (PVDF) (10 wt%) binder dispersed in *N*-methyl-2-pyrrolidone (NMP) to form a homogeneous slurry, which was then spread on Al foil and dried at 60 °C for 12h. The foil was cut into a circle of diameter 16 mm (10 mm for high sulfur loading) as the sulfur cathode. CR2032 coin cells consisting of lithium metal foil anodes, Celgard 2500 separator and the above sulfur cathodes were prepared in an argon-filled glove box. The electrolyte is composed of 1 M LiTFSI dissolved in DOL/DME (1:1, vol) with 0.1 M LiNO$_3$ additive. The areal loadings of the sulfur cathodes were 1.2 and 4.83 mg cm^{-2} (high sulfur loading) for testing, and the electrolyte/sulfur ratio is 12.43 and 13.18 μl mg^{-1}, respectively. The charge–discharge tests (based on the mass of sulfur) were carried out on a Neware battery test system at 1.7 to 2.8 V (*vs.* Li/Li$^+$). The cyclic voltammetry (CV) data and the curves of Li$_2$S nucleation are obtained with a VMP3 electrochemical workstation (Bio Logic) with a scan rate of 0.1 mV s^{-1} in 1.7–2.8 V, and the electrochemical impedance spectra (EIS) measurement was conducted at frequency ranges from 100 kHz to 10 MHz.

Theoretical calculations

The density functional theory (DFT) method was employed for simulation calculations by using the Vienna *ab initio* simulation package (VASP).[20] And the Perdew–Burke–Ernzerhof (PBE) function of the generalized gradient approximation (GGA) was described for the electronic exchange–correlation energy.[21] The kinetic cutoff energy for the plane wave basis set was 550 eV, and a $3 \times 3 \times 1$ Γ-centered k-point mesh was employed for the geometrical optimization. To eliminate the interactions between adjacent unit cells, a vacuum separation over 10 Å was added. All structures were relaxed fully to energy minimization with the force per atom below 0.01 eV Å^{-1}. The threshold of total energy was 10^{-5} eV with DFT-D2 correction to consider the van der Waals interactions. The absorption processes were evaluated on a five-layer surface model, in which the bottom three layers were fixed during the structure relaxations. The corresponding adsorption energy was calculated as follows:

$$E_{ad} = E_{total} - E_{suf} - E_{Li_2Sn} \tag{1}$$

where E_{ad}, E_{total}, E_{suf} and E_{Li_2Sn} are adsorption energy, total energy of the adsorbed systems, the energy of the clean VN or Co-VN surface slab and the energy of Li$_2$Sn under vacuum, respectively. The d band center was calculated by using the following equations:

$$\varepsilon_d = \frac{\int_{-\infty}^{\infty} n_d(\varepsilon)\varepsilon d\varepsilon}{\int_{-\infty}^{\infty} n_d(\varepsilon) d\varepsilon} \tag{2}$$

where ε is the electronic energy of states, and n is the electronic density of states. The Li$^+$ migration energy barrier on the VN and Co-VN surfaces has been evaluated by the climbing image nudged elastic band (CI-NEB) method.

Results and discussion

The preparation process of the 3D Co-VN/NC framework is schematically presented in Fig. 1. First, the NaCl crystals as a hard template, the glucose as a carbon source, and the NH$_4$VO$_3$, urea and Co(NO$_3$)$_2$·6H$_2$O as the V, N and Co sources, respectively, were all dissolved in deionized water to form a homogeneous solution. A freeze-drying process was carried out to remove the needless water, and meanwhile the NaCl crystals were uniformly coated with glucose, NH$_4$VO$_3$, urea, and Co(NO$_3$)$_2$·6H$_2$O complex together, as shown in Fig. S1a (ESI†), where the NaCl particles were aggregated into a 3D structure. By thermal treatment of the above powders and melamine at 750 °C in an Ar atmosphere, the glucose was carbonized to form a three-dimensional graphitic carbon structure with micro- and mesopores, and urea was pyrolyzed as the nitrogen source to form N-doped carbon. Meanwhile, Co-VN nanocrystals were obtained through thermal reduction of the Co-V precursor in nitrogen-rich gas of the thermolytic products of melamine. Significantly, the graphitic carbon on the NaCl crystal surface
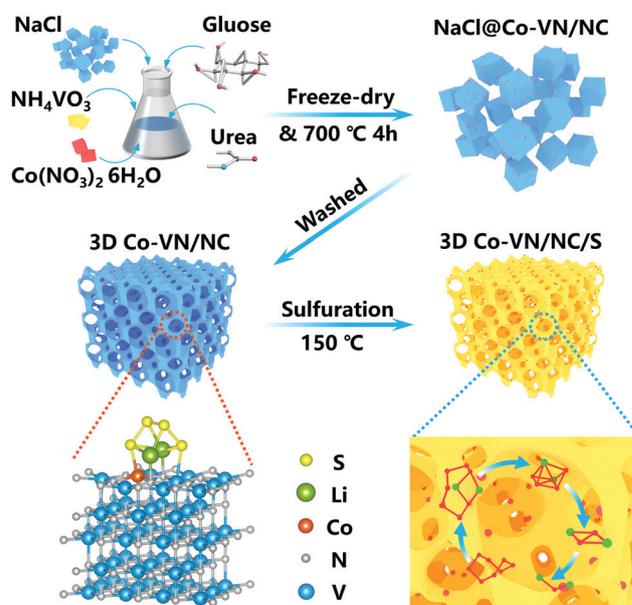

Fig. 1 Schematic illustration of the template-assisted strategy for the synthetic route of the 3D Co-VN/NC framework.

can limit the self-aggregation of VN at high pyrolysis temperatures, which can effectively increase reactive interfaces.[22] During the pyrolysis process, the original morphology of the NaCl template can be generally maintained (Fig. S1b, ESI†). After removing the NaCl crystals by washing with DI water, the 3D Co-VN/NC framework was obtained. Finally, sulfur was introduced into the hierarchical porous materials through a melt-diffusion strategy, which was designated as Co-VN/NC/S.

The surface morphologies of the NC, VN/NC and Co-VN/NC are displayed in Fig. 2. As shown in Fig. 2a1–a2, the NC sample displays a 3D porous structure consisting of an interconnected ultrathin carbon backbone. After the addition of NH_4VO_3 and $Co(NO_3)_2 \cdot 6H_2O$, the structures of VN/NC and Co-VN/NC still keep the honeycomb-like porous framework (Fig. 2b1 and c1), and the VN and Co-VN nanocrystals are uniformly distributed on the walls of graphitic carbon as shown in the higher magnification images (Fig. 2b2 and c2). Moreover, thermogravimetric analysis in Air suggests that the content of Co-VN in Co-VN/NC is about 39.9% (Fig. S2a, ESI†).[23,24] To verify the functions of melamine and urea, we also synthesized samples through similar comparative experiments. When the sample is normally annealed without adding melamine, the final product is a carbon composite material with no obvious VN crystal

particles on the surface, and the XRD test result also showed no diffraction peak of vanadium nitride (Fig. S2b and c, ESI†). The corresponding XPS data of the control sample without adding melamine are also given. The XPS spectrum (Fig. S2e and f, ESI†) demonstrates the presence of nitrogen-doped carbon in the obtained sample, but this may be due to the nitrogen source provided by urea and NH_4VO_3 ($2NH_4VO_3 \xrightarrow{\Delta} V_2O_5 + 2NH_3 \uparrow + H_2O$). The above results prove that melamine is the main nitrogen source of VN. Without urea, the synthesized sample still contains VN, but the concentration of the precursor solution changed, which led to the fracture of the three-dimensional carbon network structure (Fig. S2b and d, ESI†). In addition, considering that NH_4VO_3 can be pyrolyzed to produce NH_3, 3D NC was prepared without adding melamine, NH_4VO_3 and $Co(NO_3)_2 \cdot 6H_2O$ in the normal annealing process. And the high-resolution XPS spectra of N 1s and C 1s were obtained for the 3D NC sample, which proved that nitrogen was successfully doped into the carbon material (Fig. S2g and h, ESI†). In summary, we believe that urea is a nitrogen source of nitrogen-doped carbon and also supports the 3D structure of the carbon network.

The structural morphology of Co-VN/NC was further elucidated by TEM. As shown in Fig. 2d, the 3D network structure
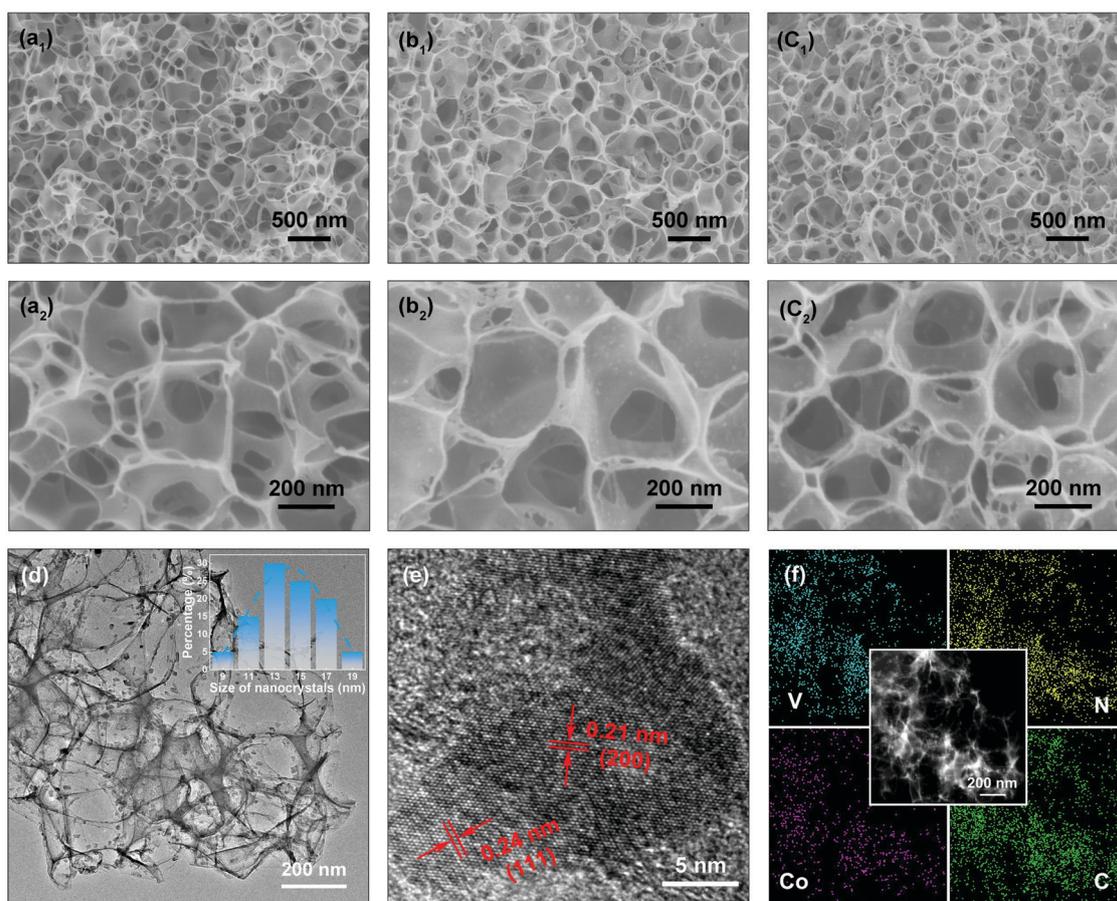

Fig. 2 (a1–a2) SEM images of N-doped graphitic carbon. (b1–b2) SEM images of VN/NC. (c1–c2) SEM images of Co-VN/NC. (d) TEM images of 3D Co-VN/NC, inset: size distribution of the Co-VN nanocrystals in 3D Co-VN/NC. (e) HRTEM images of Co-VN/NC. (f) EDS mappings of Co-VN/NC.

formed *via* the ultrathin carbon walls was robustly interspersed with Co-VN nanoparticles, which was consistent with the SEM images. And the statistical data inset of Fig. 2d indicated that the size of the Co-VN nanocrystals ranged from 9 to 20 nanometers. A representative HRTEM image is shown in Fig. 2e, disclosing lattice fringes with a spacing of 0.24 and 0.21 nm, which corresponded to the (111) and (200) planes of VN, respectively.[25,26] In addition, the elemental mapping images (Fig. 2f) reveal the homogeneous distribution of vanadium, nitrogen, cobalt and carbon elements in the 3D Co-VN/NC framework. As shown in Fig. S3 (ESI†), the energy dispersive X-ray (EDX) analysis reveals that the molar ratio of N to V elements is about 1.23 : 1, and the excess nitrogen element comes from the nitrogen-doped carbon network.

The crystal structures of the Co-VN/NC, VN/NC and NC were identified by X-ray diffraction (Fig. 3a). Four Bragg reflection peaks at 37.6°, 43.7°, 63.6°, and 76.3° are assigned to the (111), (200), (220), and (311) lattice planes, respectively.[27] All diffraction peaks were well indexed to cubic VN ($Fm3m$, JCPDS No. 73-0528), with the wide peak around 26° corresponding to amorphous carbon.[28] Meanwhile, the XRD patterns (Fig. 3b) of Co-VN/NC display peaks at 76.4°, significantly positively shifted to a higher angle compared to that of VN/NC, which is due to the atomic radius of cobalt being smaller than that of vanadium.[29,30] In addition, the intensity of the XRD peaks reduces and also becomes broader, illustrating the successful doping of Co into the VN crystal lattice.[31]

X-ray photoelectron spectroscopy (XPS) was used to investigate the surface composition information of Co-VN/NC and the nature of the dopants. The full XPS spectrum (Fig. S4a, ESI†) shows that the Co-VN/NC network consists of V, N and C elements, and an obvious peak of Co 2p can be observed, clarifying the successful Co element doping in the VN nanocrystals.[16] The high-resolution XPS spectra of Co 2p in Fig. 3c show two peaks at 796.4 and 781.2 eV, which can be attributed to the Co $2p_{1/2}$ and Co $2p_{3/2}$ doublet, respectively. The deconvoluted XPS spectrum of V 2p in Fig. S4b (ESI†) indicates the presence of V–N (514.1 eV, 522.3 eV), V–N–O (515.7 eV, 522.4 eV) and V–O (516.9 eV, 524.7 eV) bonds, and the oxygen-containing functional groups on the surface of Co-VN could play roles in anchoring LiPSs.[32] The N1s spectrum can be deconvoluted into four peaks, as shown in Fig. S4c (ESI†), and the characteristic peaks at 397.3 eV, 398.5 eV, 400.3 eV and 401.4 eV can be attributed to V-N, pyridine N, pyrrolic N, and graphite N, respectively.[33] By carefully fitting the C 1s spectrum (Fig. S4d, ESI†), three prominent peaks at 284.7 eV, 285.8 eV and 288.3 eV can be assigned to the C–C, C–N and C=O bonds, respectively.[34] The presence of C–N bonds changed the nonpolar surfaces of graphitic carbon and thus enhanced their affinity to LiPSs.[35]

In addition, the Raman scattering spectra (Fig. 3d) were obtained to confirm the degree of graphitization for the Co-VN/NC, VN/NC and NC, and two typical peaks around 1340 (D-band) and 1590 cm^{-1} (G-band) indicate the existence of disordered carbon and graphitic carbon, respectively.[36,37] The intensity ratio (I_D/I_G) of Co-VN/NC, VN/NC and NC was characterized as 0.934, 0.956 and 0.866, respectively, indicating a high graphitization degree, which can enhance the electrical conductivity of the composites. The pore structure characteristics of the 3D Co-VN/NC framework were investigated using N$_2$ adsorption–desorption measurements, as shown in Fig. 3e, and the corresponding specific surface area for the prepared sample is 119 m^2 g^{-1}. The type IV isotherm and the pore size distribution together imply the coexistence of micro-, meso-, and macropores in the Co-VN/NC.[22,38] The micropores afford higher adsorption energy for physically restricting LiPSs in the
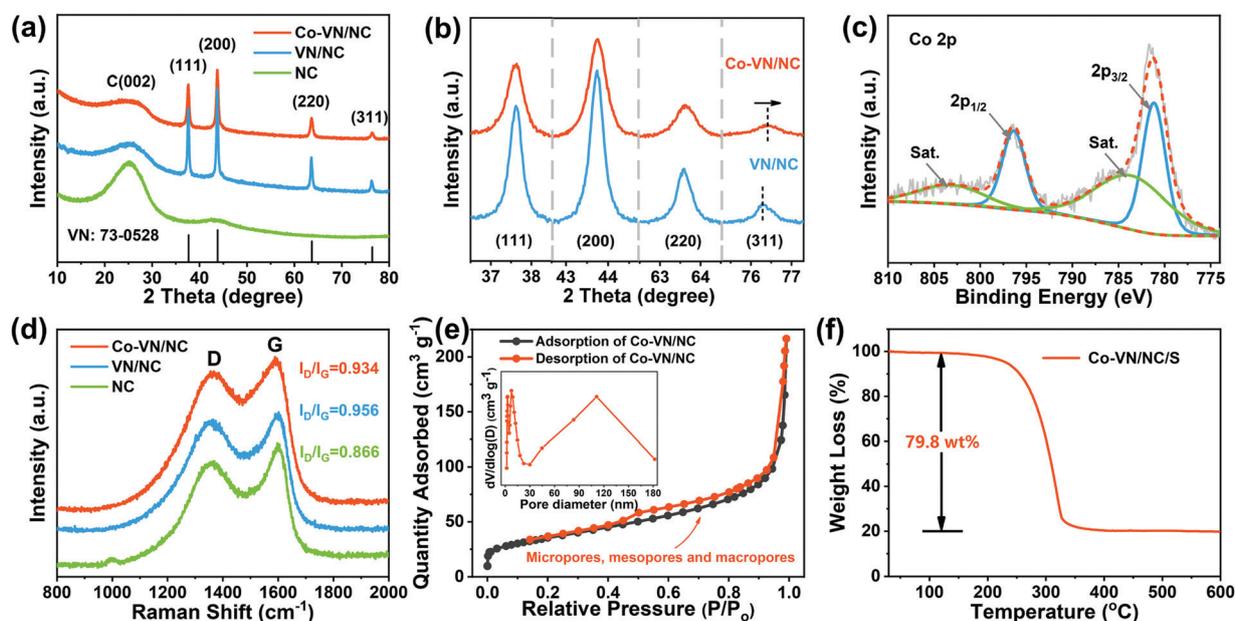

Fig. 3 (a and b) XRD patterns of Co-VN/NC, VN/NC and NC. (c) Refined XPS spectra of Co 2p for Co-VN/NC. (d) Raman spectra of the three materials. (e) N$_2$ adsorption/desorption isotherms and pore size distributions of Co-VN/NC. (f) TG curves of the Co-VN/NC/S composites.

cathode, the existence of mesopores provides an appropriate length of ionic/electric diffusion path for LiPS conversion, and the macropores expose lots of Co-VN particles and accommodate the high sulfur loading of the cathode.[39] The thermogravimetric analysis (TGA) profile of Co-VN/NC/S in Fig. 3f shows that the sulfur content is about 79.8 wt%, and the corresponding XRD patterns of the porous materials after sulfur was incorporated are shown in Fig. S5a (ESI†), which display typical peaks indexed to S_8 (JCPDS: 08-0247).[40] Meanwhile, the fact that sulfur was uniformly distributed on the surface of the 3D Co-VN/NC framework can be verified by SEM (Figure S5b and c, ESI†).

The strong chemical adsorption of the 3D Co-VN/NC framework to LiPSs was verified by adding 5 mg of the host material to 5 mM Li_2S_6 solution (3 ml). As shown in Fig. 4a, the brown polysulfide solution containing Co-VN/NC became nearly colorless after 2 h, while the color of the VN/NC sample solutions just lightened slightly and the solution with NC still kept a brown color, suggesting that the anchoring capability of VN has been enhanced after cobalt doping. Moreover, ultraviolet-visible (UV-Vis) adsorption tests further verified the role of cobalt doping in polysulfide entrapment. It is clear that the absorbance peak of the solution with Co-VN/NC almost disappears in the 400–500 nm range, which dramatically confirms that the Co-VN/NC framework possesses excellent adsorption capability toward LiPSs due to the strong polar nature of the Co dopants.[41] XPS spectra of Co-VN/NC after soaking in Li_2S_6 solutions were collected (Fig. 4b). The Co $2p_{1/2}$ and $2p_{3/2}$ peaks of the Co-VN/NC/Li_2S_6 showed a significant negative shift, indicating that the strong interaction between LiPSs and Co

increased the electron density at the metal center, which implies the formation of Co–S bonds.[42]

To further explore the in-depth effect of Co doping of VN to achieve efficient polysulfide trapping and redox kinetics, density functional theory (DFT) calculations were carried out. Fig. 4c shows the partial densities of states (PDOS) for V, N and Co atoms of VN and Co-VN, and there is no energy gap near to the Fermi level after cobalt doping, which indicates the metallic nature of Co-VN.[33] Impressively, the Co-VN exhibited a higher V d band center (−0.730) compared with that of VN (−0.768), suggesting that the doped cobalt embellishes the electronic structure of VN and enhances the adsorption ability toward polysulfides.[43] And the d band center of Co-VN with different Co doping ratios was also calculated, and the calculation results display that the d band center was increased first and then decreased when subjected to increasing Co doping levels (Fig. S6, ESI†). Then, the optimal geometric structures of Li_2S_n (n = 1, 2, 4, 6, 8) adsorbed on the Co-VN surfaces are provided in Fig. 4e, and the formed Co–S bond indicates that the Co atom can adsorb the polysulfides.[44] The adsorption energy (E_a) calculation results are indicated in Fig. 4d, and the E_a values for Co-VN with Li_2S, Li_2S_2, Li_2S_4, Li_2S_6, and Li_2S_8 species are −2.29, −2.69, −2.47, −2.69 and −2.68 eV, respectively, which are obviously higher than those of VN (our previous work).[40] This is due to the d electron transfer from Co ions to VN; the changing coordination environment of VN causes more active sites to be exposed, which promotes the interactions between electron-rich VN and LiPSs as well as sulfur redox kinetics.[45]
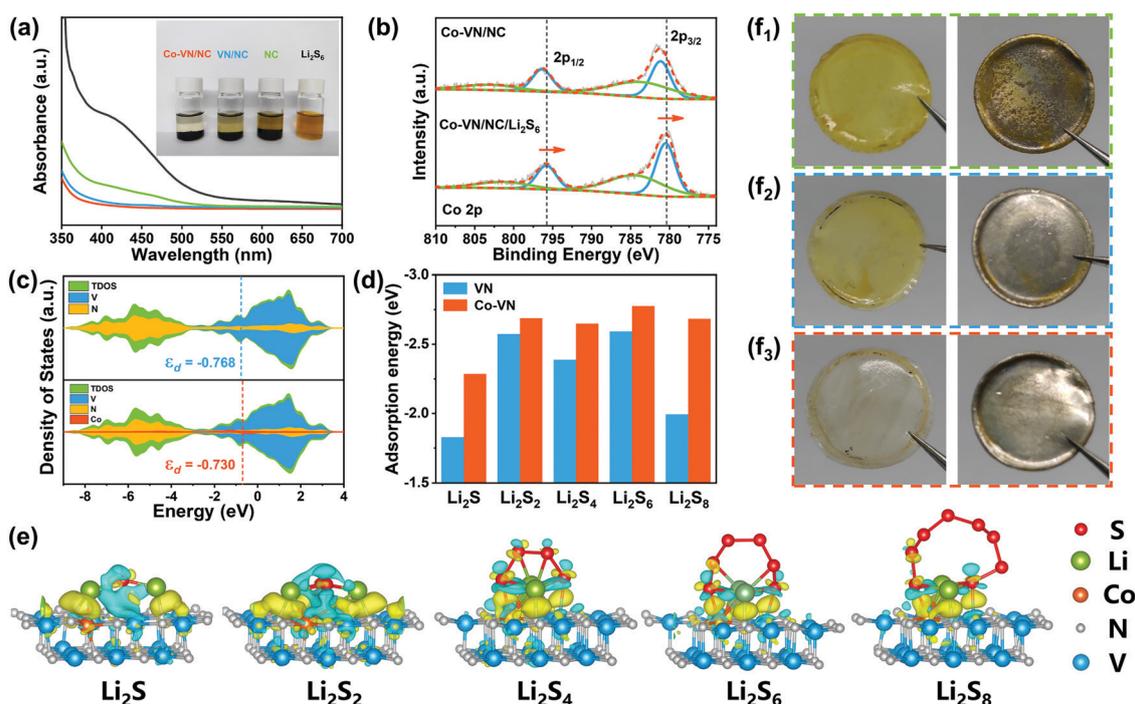

Fig. 4 (a) UV-vis spectra of Li_2S_6 solution and ones after adding the Co-VN/NC, VN/NC and NC catalysts. Inset: Visualized adsorption test. (b) XPS Co_{2p} spectrum of Co-VN/NC after Li_2S_6 adsorption. (c) The density of states spectrum of Co-VN and VN. (d) Adsorption energy between sulfur species and Co-VN or VN on the (200) plane. (e) The optimized configurations of the Li_2S_n (n =1, 2, 4, 6, and 8) molecules adsorbed on the surface of Co-VN. Photographs of the separators and lithium foils in the NC (f_1), VN/NC (f_2) and Co-VN/NC (f_3) cells.

In addition, the separators and lithium anodes in different batteries after 50 cycles were disassembled. As shown in Fig. 4f1–2, there are apparent yellow LiPSs on the separator of the NC and VN/NC cathode, and the surfaces of the corresponding lithium foils were corroded, indicating a certain amount of LiPS shuttling to the anode.[28,46] As seen from Fig. 4f3, the 3D Co-VN/NC framework can effectively relieve the shuttle effect, and these results further strongly demonstrate the enhanced trapping capability of VN after Co doping.

Apart from the effective adsorption effect, we also investigated the electrocatalytic reaction kinetics for cobalt-doped VN, and the lithium-ion diffusion coefficient (D_{Li}) was analyzed through cyclic voltammetry (CV) testing of the Co-VN/NC/S, VN/NC/S and NC/S cathodes (Fig. 5a and Fig. S7a, b, ESI†). The D_{Li} values for the different electrodes were calculated according to the Randles–Sevcik equation:

$$I_{peak} = (2.69 \times 10^5)n^{1.5}AD_{Li}^{0.5}v^{0.5}C_{Li} \tag{3}$$

where I_{peak} is the peak current (A), n represents electron number in the electrochemical reaction (n = 2 for Li-S batteries), A represents the geometrical area of the electrode (2 cm^2), D_{Li} is the Li$^+$ diffusion coefficient (cm^2 s^{-1}), v is the scan rate of the CV tests (V s^{-1}) and C_{Li} is the concentration of Li$^+$ in the electrolyte (0.55 mol L^{-1}).[47] As indicated in Fig. S7d–f (ESI†), all anodic and cathodic peak currents (I_{peak}) show an excellent linear relationship with the square root of the scan rates ($v^{0.5}$). Apparently, the Co-VN/NC/S cathode exhibits much higher slopes than its counterparts, exhibiting the largest Li$^+$ diffusion values for all redox peaks, indicating the accelerated diffusion process and enhanced conversion kinetics for polysulfides (Fig. 5b and Table S1, ESI†). Thereafter, the Tafel slopes of the reduction (Li$_2$S$_n$ to Li$_2$S) and oxidation (from Li$_2$S to S$_8$) peaks derived from the CV tests were calculated, as shown in Fig. 5c and d. Evidently, the Co-VN/NC/S cathode exhibits the lowest Tafel slope values of the oxidation and reduction processes, indicating its remarkable bidirectional catalytic ability for the efficient redox conversion between LiPSs and Li$_2$S.[48] In addition, the Co-VN/NC cell also displays lower ohmic resistance and charge transfer resistance indicating fast synergetic catalytic conversion of LiPSs by the cobalt-doped VN host (Fig. S7c, ESI†).

To further verify the electrocatalytic effects, the contribution of cobalt doping to the improved conversion kinetics of LiPSs was confirmed by the symmetric cell tests. As illustrated in Fig. 5e, the voltammogram of Co-VN/NC without Li$_2$S$_6$ shows negligible capacitance, and the NC electrode shows only a pair of broad redox peaks with a large peak separation, indicating
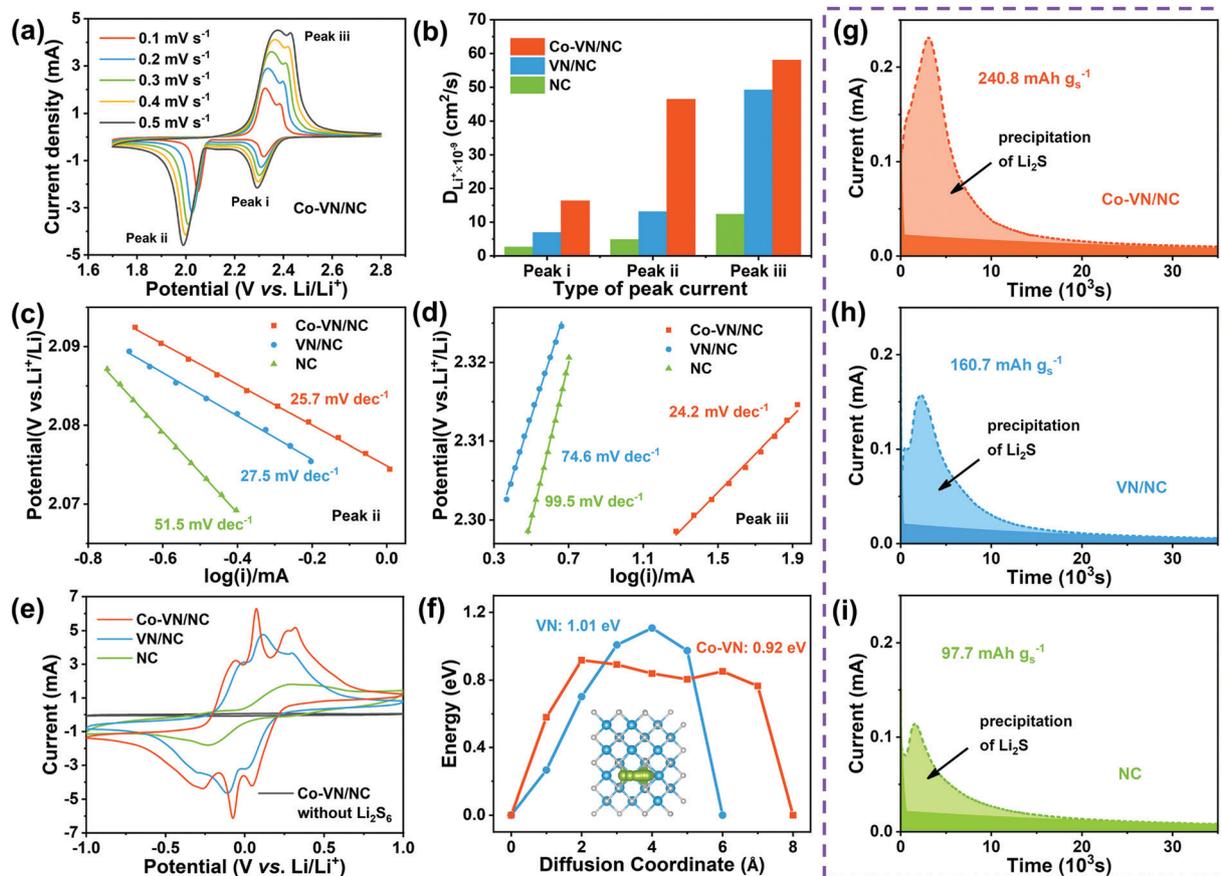

Fig. 5 (a) CV curves of Co-VN/NC electrodes at scan rates from 0.1 to 0.5 mV s^{-1}. (b) Diffusion coefficient of Li ions of Co-VN/NC, VN/NC and NC electrodes for peak i, ii, and iii processes. (c and d) Tafel plots corresponding to peak ii and iii with the different cathode composites. (e) CV curves obtained at 1 mV s^{-1} for the Li$_2$S$_6$ symmetric cells using Co-VN/NC, VN/NC and NC as electrodes, respectively. (f) Energy barriers of Li$^+$ diffusion on the Co-VN and VN (200) plane. (g–i) Potentiostatic discharge curves of Li$_2$S$_8$ solution on the surfaces of the Co-VN/NC, VN/NC and NC.

the poor reaction kinetics. In contrast, the Co-VN/NC and VN/NC electrodes with Li_2S_6 both clearly display three pairs of redox peaks, and the peaks around $-0.05/0.05V$, $-0.27/0.27V$ and $-0.07/0.07V$ represent the reversible stepwise redox reactions of $Li_2S_6 \leftrightarrows Li_2S_4$, $Li_2S_4 \leftrightarrows Li_2S_2/Li_2S$, and $S_8 \leftrightarrows Li_2S_6$, respectively.[49,50] Moreover, the Co-VN/NC cell exhibits smaller peak separation and higher current intensity relative to VN/NC, implying the significantly boosted conversion kinetics between LiPSs and Li_2S, which is ascribed to the catalytic effects of the dopant cobalt element. To gain insight into the catalytic processes of the 3D Co-VN/NC framework for polysulfide conversion, the calculation of the Li ion diffusion pathways on both the Co-VN and VN surfaces was further implemented and the results are shown in Fig. 5f. The energy barrier of the Li ion along the diffusion coordinate on Co-VN is 0.92 eV, which is lower than that on VN (1.01 eV), reflecting the faster interfacial ion transfer dynamics of VN after cobalt doping, which can dramatically facilitate the reversible conversion of LiPSs during oxidation–reduction processes.[51,52] And the diffusion pathways of Li ions on Co-VN and VN surfaces are displayed in Fig. 5f and Fig. S8 (ESI†), respectively. The nucleation experiments of Li_2S on the Co-VN/NC, VN/NC and NC catalysts further demonstrate the enhanced LiPS conversion (Fig. 5g–i).[24,53] According to Faraday's law, Co-VN/NC shows the largest capacity of Li_2S

precipitation (240.8 mA h g^{-1}), which is much higher than that of VN/NC (160.7 mA h g^{-1}) and NC (97.7 mA h g^{-1}), implying that Co-VN/NC can significantly promote the reduction of LiPSs. Moreover, the nucleation experiments of Li_2S on Co-VN/NC with different Co doping contents were also studied, the results show that the activity of Li_2S precipitation was the highest when the Co doping content in Co-VN was 3 at% (Fig. S9a–d, ESI†).

The electrochemical properties of Co-VN/NC, VN/NC and NC as the sulfur host were systematically evaluated in the following research. Fig. 6a displays the typical CV curves of different electrodes between 1.7 and 2.8 V at a sweep rate of 0.1 mV s^{-1}. A pair of reduction peaks are observed during the discharge process, assigned to the reduction of sulfur to long-chain LiPSs at higher voltage and the formation of insoluble Li_2S_2/Li_2S at a lower voltage, respectively.[54] Besides, two overlapped oxidation peaks during the charging process stand for the conversions from Li_2S_2/Li_2S to lithium polysulfides and finally to sulfur.[55] Compared to the VN/NC and NC electrodes, the CV curve of the Co-VN/NC exhibits a positive shift of the reduction peaks and a negative shift of the oxidation peak, representing the less polarization and benign reversibility.[4] In other words, due to the synergistic electrocatalytic effects of cobalt doping VN nanocrystals, the Co-VN/NC electrodes exhibited the sharpest peak currents and smallest polarization compared to the VN/NC and
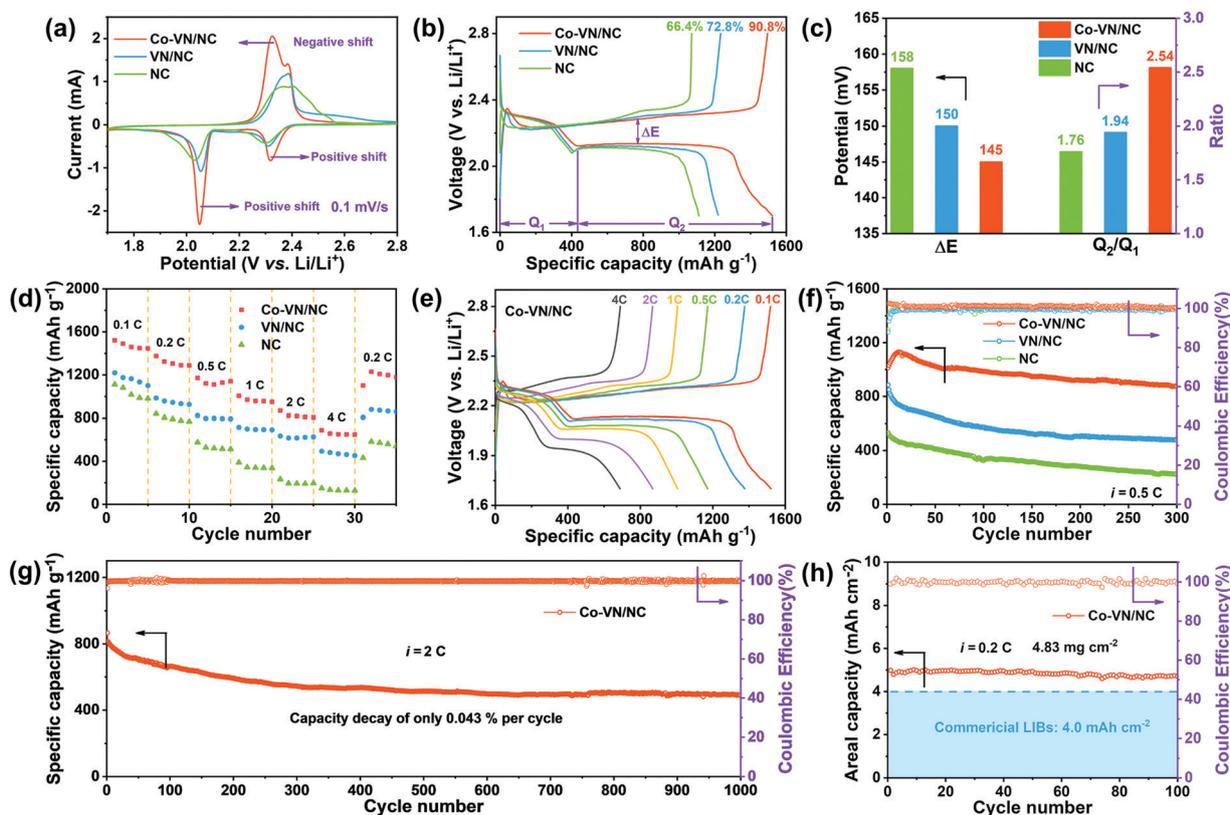

Fig. 6 (a) Typical CV profiles of Co-VN/NC, VN/NC and NC electrodes at 0.1 mV s^{-1}. (b) The first charge–discharge curves obtained at 0.1 C with the different cathode composites. (c) Corresponding voltage gap (ΔE) and Q_2/Q_1 values obtained from charge–discharge curves. (d) Rate capability of the Co-VN/NC, VN/NC and NC electrodes at various current rates from 0.2 to 4 C. (e) Galvanostatic charge–discharge curves of the Co-VN/NC electrodes at various current densities. (f) Comparative cycling stability of the three different cathodes at 0.5 C. (g) Long-term cycling performance at 2 C of the Co-VN/NC electrodes. (h) Cycling performance of the Co-VN/NC electrodes with high sulfur loading at 0.2 C.

Nanoscale Horizons

View Article Online

Communication

NC. At the same time, the charge–discharge voltage plots of different cathodes are shown in Fig. 6b. Compared to the initial capacity of the cathodes with VN/NC (1219 mA h g^{-1}) and NC (1111 mA h g^{-1}), the Co-VN/NC cathode exhibits much larger capacity of 1521 mA h g^{-1}, and much higher sulfur utilization of 90.8% (based on the theoretical value of sulfur, 1675 mA h g^{-1}).[56] Additionally, we calculated the polarization potential (ΔE) between the oxidation and reduction plateau in Fig. 6c, and the Co-VN/NC cathode shows a smaller plateau voltage gap (ΔE = 145 mV) than the VN/NC (ΔE = 150 mV) and NC (ΔE = 158 mV) cathodes, representing higher reversibility and more efficient conversion kinetics of sulfur redox reactions.[57] The discharge capacity ratio of low and high voltage plateaus (Q_2/Q_1) was calculated to explain the kinetics of the reduction process as illustrated in Fig. 6c. It is clear that the Q_2/Q_1 ratio of the Co-VN/NC cathode (2.54) is much higher than that of VN/NC (1.94) and NC (1.76), further revealing that the Co-VN electrocatalyst can effectively propel the reaction kinetics of liquid–solid conversion.[58]

The rate capabilities of the cells with Co-VN/NC, VN/NC and NC cathodes were evaluated from 0.1 to 4 C and returning to 0.2 C (Fig. 6d). Compared with other cathodes, the Co-VN/NC cathode displays superior capacities of 1172, and 688 mA h g^{-1} at 0.5 and 4 C, respectively, and achieves a high capacity of 1229 mA h g^{-1} even when the current density returns to 0.2 C. Fig. 6e exhibits the galvanostatic charge and discharge curves of the Co-VN/NC cathode at different current rates, and the discharge profiles distinctly show two-reductive-plateaus even though the current density is at 4 C, which further demonstrates that the Co-VN/NC electrocatalyst achieves excellent reaction kinetics. After the rate tests, the comparative cycling stability of these cells was measured at 0.5 C (Fig. 6f). After 300 cycles, the Co-VN/NC cathode retained a high reversible capacity of 876 mA h g^{-1} with a capacity retention of 86.5%. In comparison, the VN/NC and NC cathodes present discharge capacities of 478 and 225 mA h g^{-1} after 300 cycles, respectively. Fig. 6g demonstrates the long-term cycling performance of the Co-VN/NC cathode at 2 C over 1000 cycles, delivering a remarkable capacity retention of ∼490 mA h g^{-1} with a low capacity decay of 0.043% for each cycle, and a Coulombic efficiency of nearly 100% in all the cycles. In order to evaluate the commercialized applications of Co-VN/NC, Li–S batteries with high sulfur loading were investigated (4.83 mg cm^{-2}). As displayed in Fig. 6h, the cell delivers an excellent initial area-specific capacity of 4.98 mA h cm^{-2} and retains 4.70 mA h cm^{-2} (94.3%) after 100 cycles at 0.2 C, which is higher than that of commercial lithium-ion batteries (4.0 mA h cm^{-2}).[59,60] Compared with other previously reported host materials for Li–S batteries (Table S2, ESI†), the electrochemical performance of the 3D Co-VN/NC cathode exceeds most relevant studies, indicating the outstanding advantage of cobalt-doped VN nanocrystals as high-performance hosts for a lithium–sulfur battery.

Conclusion

In summary, we rationally designed a porous conductive framework embedded with cobalt-doped vanadium nitride nanocrystals by a facile template-assisted strategy as an efficient polysulfide adsorber and convertor for Li–S batteries. The widespread ultrasmall Co-VN particles and hierarchical porous graphitic carbon network offer abundant triple-phase interfaces and contact sites for rapid surface reactions of LiPSs. Density functional theory calculations and experimental results jointly demonstrated the enriched d orbit electrons and embellished bandgap of VN by cobalt doping, and further improved the anchoring ability and catalytic activity of the Co-VN/NC host to LiPSs. Benefiting from the enhanced chemical affinity and fast catalytic conversion, the 3D Co-VN/NC cathodes exhibit excellent cycling stability with a low decay rate of 0.043% per cycle over 1000 cycles at 2.0 C. More importantly, our 3D Co-VN/NC host delivered a high areal capacity of 4.98 mA h cm^{-2} even with a sulfur loading of 4.83 mg cm^{-2}. This metal doping strategy provides a unique insight for constructing different catalysts with optimized trapping and conversion activity in Li–S batteries.

Conflicts of interest

There are no conflicts to declare.

Acknowledgements

References

1 B. Chen, D. S. Wang, B. Zhang, X. W. Zhong, Y. Q. Liu, J. Z. Sheng, Q. Zhang, X. L. Zou, G. M. Zhou and H. M. Cheng, *ACS Nano*, 2021, **15**, 9841–9850.
2 M. Rebber, C. Willa and D. Koziej, *Nanoscale Horiz.*, 2020, **5**, 431–453.
3 E. Cha, M. Patel, S. Bhoyate, V. Prasad and W. Choi, *Nanoscale Horiz.*, 2020, **5**, 808–831.
4 Y. Z. Song, Z. T. Sun, Z. D. Fan, W. L. Cai, Y. L. Shao, G. Sheng, M. L. Wang, L. X. Song, Z. F. Liu, Q. Zhang and J. Y. Sun, *Nano Energy*, 2020, **70**, 104555.
5 S. J. Kim, Y. Jeoun, J. Park, S. H. Yu and Y. E. Sung, *Nanoscale*, 2020, **12**, 15466–15472.
6 Y. Yao, H. Y. Wang, H. Yang, S. F. Zeng, R. Xu, F. F. Liu, P. C. Shi, Y. Z. Feng, K. Wang, W. J. Yang, X. J. Wu, W. Luo and Y. Yu, *Adv. Mater.*, 2020, **32**, 1905658.
7 M. B. Zheng, Y. Chi, Q. Hu, H. Tang, X. L. Jiang, L. Zhang, S. T. Zhang, H. Pang and Q. Xu, *J. Mater. Chem. A*, 2019, **7**, 17204–17241.
8 M. R. Li, H. Y. Peng, Y. Pei, F. Wang, Y. Zhu, R. Y. Shi, X. X. He, Z. B. Lei, Z. H. Liu and J. Sun, *Nanoscale*, 2020, **12**, 23636–23644.

9 T. Peng, N. Zhang, Y. B. Wang, M. L. Zhao, W. W. Sun, D. Y. Zhang, H. L. Yan, Y. Lu and Y. S. Luo, *J. Solid State Electrochem.*, 2020, **25**, 505–512.

10 R. J. Luo, Q. H. Yu, Y. Lu, M. J. Zhang, T. Peng, H. L. Yan, X. M. Liu, J. K. Kim and Y. S. Luo, *Nanoscale Horiz.*, 2019, **4**, 531–539.

11 Y. G. Zhang, Y. G. Wang, R. J. Luo, Y. Yang, Y. Lu, Y. Guo, X. M. Liu, S. X. Cao, J. K. Kim and Y. S. Luo, *Nanoscale Horiz.*, 2020, **5**, 530–540.

12 Z. H. Sun, J. Q. Zhang, L. C. Yin, G. J. Hu, R. P. Fang, H. M. Cheng and F. Li, *Nat. Commun.*, 2017, **8**, 14627.

13 N. Li, Z. M. Xu, P. Wang, Z. A. Zhang, B. Hong, J. Li and Y. Q. Lai, *Chem. Eng. J.*, 2020, **398**, 125432.

14 Y. Z. Song, W. Zhao, L. Kong, L. Zhang, X. Y. Zhu, Y. L. Shao, F. Ding, Q. Zhang, J. Y. Sun and Z. F. Liu, *Energy Environ. Sci.*, 2018, **11**, 2620–2630.

15 H. Yang, Y. Hu, D. Huang, T. Xiong, M. Li, M. S. Balogun and Y. Tong, *Mater. Today Chem.*, 2019, **11**, 1–7.

16 N. Zhang, L. Y. Cao, L. L. Feng, J. F. Huang, K. Kajiyoshi, C. Y. Li, Q. Q. Liu, D. Yang and J. J. He, *Nanoscale*, 2019, **11**, 11542–11549.

17 Q. F. Zhang, Z. S. Qiao, X. R. Cao, B. H. Qu, J. Yuan, T. E. Fan, H. F. Zheng, J. Q. Cui, S. Q. Wu, Q. S. Xie and D. L. Peng, *Nanoscale Horiz.*, 2020, **5**, 720–729.

18 W. J. Ren, L. Q. Xu, L. Zhu, X. Y. Wang, X. J. Ma and D. B. Wang, *ACS Appl. Mater. Interfaces*, 2018, **10**, 11642–11651.

19 Z. Z. Cheng, Y. X. Wang, W. J. Zhang and M. Xu, *ACS Appl. Energy Mater.*, 2020, **3**, 4523–4530.

20 G. Kresse and J. Furthmüller, *Comput. Mater. Sci.*, 1996, **6**, 15–50.

21 J. P. Perdew, K. Burke and M. Ernzerhof, *Phys. Rev. Lett.*, 1996, **77**, 3865.

22 Q. H. Yu, Y. Lu, R. J. Luo, X. M. Liu, K. F. Huo, J.-K. Kim, J. He and Y. S. Luo, *Adv. Funct. Mater.*, 2018, **28**, 1804520.

23 X. S. Xu, Y. X. Xu, F. Xu, G. S. Jiang, J. Jian, H. W. Yu, E. M. Zhang, D. Shchukin, S. Kaskel and H. Q. Wang, *J. Mater. Chem. A*, 2020, **8**, 1636–1645.

24 X. S. Xu, F. Xu, C. Z. Qu, G. S. Jiang, H. Q. Yu, H. Repich, H. J. Han, F. R. Cao, L. Li and H. Q. Wang, *Adv. Funct. Mater.*, 2021, 2101059.

25 Y. Zhong, D. L. Chao, S. J. Deng, J. Y. Zhan, R. Y. Fang, Y. Xia, Y. D. Wang, X. L. Wang, X. H. Xia and J. P. Tu, *Adv. Funct. Mater.*, 2018, **28**, 1706391.

26 Y. D. Yang, X. X. Li, R. J. Luo, X. M. Zhang, J. J. Fu, Y. Zheng, K. F. Huo and T. F. Zhou, *Mater. Chem. Front.*, 2021, **5**, 3830–3840.

27 T. Peng, Y. Guo, Y. G. Zhang, Y. G. Wang, D. Y. Zhang, Y. Yang, Y. Lu, X. M. Liu, P. K. Chu and Y. S. Luo, *Appl. Surf. Sci.*, 2021, **536**, 147982.

28 J. Y. Xia, W. X. Hua, L. Wang, Y. F. Sun, C. N. Geng, C. Zhang, W. C. Wang, Y. Wan and Q. H. Yang, *Adv. Funct. Mater.*, 2021, **31**, 2101980.

29 U. Godavarti, V. D. Mote and M. Dasari, *J. Australas. Ceram. Soc.*, 2017, **5**, 391–396.

30 P. W. Chen, K. Li, Y. X. Yu and W. D. Zhang, *Appl. Surf. Sci.*, 2017, **392**, 608–615.

31 Y. H. Xiao, G. H. Zhan, Z. G. Fu, Z. C. Pan, C. M. Xiao, S. K. Wu, C. Chen, G. H. Hu and Z. G. Wei, *J. Power Sources*, 2015, **284**, 296–304.

32 X. Peng, L. Wang, L. S. Hu, Y. Li, B. Gao, H. Song, C. Huang, X. M. Zhang, J. J. Fu, K. F. Huo and P. K. Chu, *Nano Energy*, 2017, **34**, 1–7.

33 S. S. Tan, Y. H. Dai, Y. L. Jiang, Q. L. Wei, G. B. Zhang, F. Y. Xiong, X. Q. Zhu, Z. Y. Hu, L. Zhou, Y. C. Jin, K. Kanamura, Q. Y. An and L. Q. Mai, *Adv. Funct. Mater.*, 2021, **31**, 2008034.

34 Z. L. Li, Z. B. Xiao, P. Y. Li, X. P. Meng and R. H. Wang, *Small*, 2020, **16**, 201906114.

35 Q. H. Li, J. Yang, Y. Zhao, Z. C. Zhang, C. Wang, H. He, J. H. Wu and X. Y. Yao, *New J. Chem.*, 2020, **44**, 5965–5971.

36 Y. Guo, L. Cao, C. Chen, Y. Lu, R. J. Luo, Q. H. Yu, Y. G. Zhang, Y. G. Wang, X. M. Liu and Y. S. Luo, *ChemistrySelect*, 2018, **3**, 5883–5890.

37 D. Sui, L. Q. Xu, H. T. Zhang, Z. H. Sun, B. Kan, Y. F. Ma and Y. S. Chen, *Carbon*, 2020, **157**, 656–662.

38 X. Y. Yang, S. Chen, W. B. Gong, X. D. Meng, J. P. Ma, J. Zhang, L. R. Zheng, H. D. Abruna and J. X. Geng, *Small*, 2020, **16**, 2004950.

39 Z. X. Zhao, Z. L. Yi, H. J. Li, R. Pathak, Z. W. Yang, X. M. Wang and Q. Q. Qiao, *Nano Energy*, 2021, **81**, 105621.

40 M. L. Zhao, Y. Lu, Y. Yang, M. J. Zhang, Z. J. Yue, N. Zhang, T. Peng, X. M. Liu and Y. S. Luo, *Nanoscale*, 2021, **13**, 13085–13094.

41 Y. G. Wang, R. J. Luo, Y. G. Zhang, Y. Guo, Y. Lu, X. M. Liu, J.-K. Kim and Y. S. Luo, *ACS Appl. Energy Mater.*, 2019, **2**, 3314–3322.

42 W. Liu, C. Luo, S. W. Zhang, B. Zhang, J. B. Ma, X. L. Wang, W. H. Liu, Z. J. Li, Q. H. Yang and W. Lv, *ACS Nano*, 2021, **15**, 7491–7499.

43 Y. G. Zhang, G. R. Li, J. Y. Wang, G. L. Cui, X. L. Wei, L. L. Shui, K. Kempa, G. F. Zhou, X. Wang and Z. W. Chen, *Adv. Funct. Mater.*, 2020, **30**, 2001165.

44 R. Q. Liu, W. H. Liu, Y. L. Bu, W. W. Yang, C. Wang, C. Priest, Z. W. Liu, Y. Z. Wang, J. Y. Chen, Y. H. Wang, J. Cheng, X. J. Lin, X. M. Feng, G. Wu, Y. W. Ma and W. Huang, *ACS Nano*, 2020, **14**, 17308–17320.

45 W. Wang, L. Y. Huai, S. Y. Wu, J. W. Shan, J. L. Zhu, Z. G. Liu, L. G. Yue and Y. Y. Li, *ACS Nano*, 2021, **15**, 11619–11633.

46 L. Zhang, Y. C. Liu, Z. D. Zhao, P. L. Jiang, T. Zhang, M. X. Li, S. X. Pan, T. Y. Tang, T. Q. Wu, P. Y. Liu, Y. L. Hou and H. B. Lu, *ACS Nano*, 2020, **14**, 8495–8507.

47 H. Y. Zhang, H. T. Cui, J. Li, Y. Y. Liu, Y. Z. Yang and M. R. Wang, *Nanoscale*, 2019, **11**, 21532–21541.

48 R. C. Wang, C. Luo, T. S. Wang, G. M. Zhou, Y. Q. Deng, Y. B. He, Q. F. Zhang, F. Y. Kang, W. Lv and Q. H. Yang, *Adv. Mater.*, 2020, **32**, 2000315.

49 G. Y. Jin, H. C. He, J. Wu, M. Y. Zhang, Y. J. Li and Y. N. Liu, *J. Inorg. Mater.*, 2021, **36**, 203–209.

50 E. D. Jing, L. Chen, S. D. Xu, W. Z. Tian, D. Zhang, N. N. Wang, Z. C. Bai, X. X. Zhou, S. B. Liu, D. H. Duan and X. Y. Qiu, *J. Energy Chem.*, 2022, **64**, 574–582.

51 S. Z. Wang, S. P. Feng, J. W. Liang, Q. M. Su, F. P. Zhao, H. J. Song, M. Zheng, Q. Sun, Z. X. Song, X. H. Jia, J. Yang,

Y. Li, J. X. Liao, R. Y. Li and X. L. Sun, *Adv. Energy Mater.*, 2021, **11**, 2003314.

52 T. H. Zhou, W. Lv, J. Li, G. M. Zhou, Y. Zhao, S. X. Fan, B. L. Liu, B. H. Li, F. Y. Kang and Q. H. Yang, *Energy Environ. Sci.*, 2017, **10**, 1694–1703.

53 F. Y. Fan, W. C. Carter and Y. M. Chiang, *Adv. Mater.*, 2015, **27**, 5203–5209.

54 L. Su, J. Q. Zhang, Y. Chen, W. Yang, J. Wang, Z. P. Ma, G. J. Shao and G. X. Wang, *Nano Energy*, 2021, **85**, 105981.

55 R. Wang, J. L. Yang, X. Chen, Y. Zhao, W. G. Zhao, G. Y. Qian, S. N. Li, Y. G. Xiao, H. Chen, Y. S. Ye, G. M. Zhou and F. Pan, *Adv. Energy Mater.*, 2020, **10**, 1903550.

56 G. X. Li, J. H. Sun, W. P. Hou, S. D. Jiang, Y. Huang and J. X. Geng, *Nat. Commun.*, 2016, 7, 10601.

57 M. L. Yu, S. Zhou, Z. Y. Wang, W. Pei, X. J. Liu, C. Liu, C. L. Yan, X. Y. Meng, S. Wang, J. J. Zhao and J. S. Qiu, *Adv. Funct. Mater.*, 2019, **29**, 1905986.

58 Z. S. Jin, T. N. Lin, H. F. Jia, B. Q. Liu, Q. Zhang, L. Li, L. Y. Zhang, Z. M. Su and C. G. Wang, *ACS Nano*, 2021, **15**, 7318–7327.

59 J. S. Cai, J. Jin, Z. D. Fan, C. Li, Z. X. Shi, J. Y. Sun and Z. F. Liu, *Adv. Mater.*, 2020, **32**, 2005967.

60 Y. Y. Wang, Z. W. Zhao, Y. Liu, L. R. Hou and C. Z. Yuan, *Rare Met.*, 2020, **39**, 1082–1091.